**Power Electronic Systems
Laboratory**

Concept of a 150 krpm Bearingless Slotless Disc Drive with Combined Windings

D. Steinert,
T. Nussbaumer,
J. W. Kolar

ETH

Eidgenössische Technische Hochschule Zürich
Swiss Federal Institute of Technology Zurich

Concept of a 150 krpm Bearingless Slotless Disc Drive with Combined Windings

Daniel Steinert, *Student Member, IEEE,* Thomas Nussbaumer, *Member, IEEE,* and
Johann W. Kolar, *Fellow, IEEE*

Abstract— **In this paper, a concept is developed for a slotless bearingless disc drive with toroidal windings for a rotational speed of 150'000 rpm. The topology and its working principles are explained and an already running prototype for lower speeds is introduced. To reach the high rotational speeds, the mechanical strength and the maximal diameter of the rotor is evaluated. Outgoing form the prototype, scaling laws are examined to identify the challenges for down-scaling of the bearingless motor. 3D FEM Simulations and optimizations are conducted to determine the influence of the magnetic gap length and to find the optimal stator and rotor height. At the end, the geometry of the high speed concept is presented and the performance results are compared to the prototype.**

*Index Terms—***bearingless motor, slotless, toroidal windings, scaling laws**
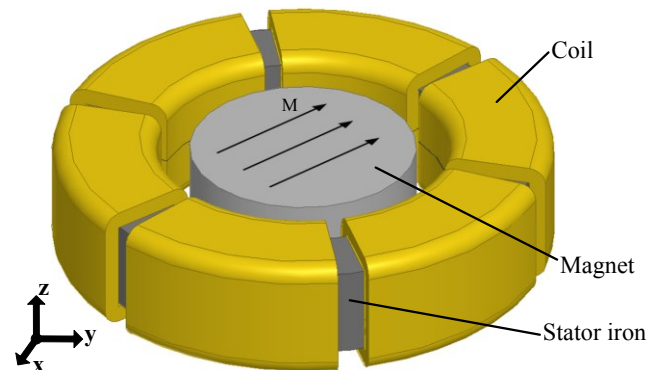
Fig. 1. Principle setup of the slotless disc motor: The rotor consists of a diametrically magnetized disc magnet. The annular rotor has six toroidally wound coils for force and torque generation.

I. INTRODUCTION

BEARINGLESS motors are used for example in applications, where high rotational speeds [1], high purity [2] or hygienic requirements [3] or chemical resistance [4] are demanded. In this paper, a concept is derived for a bearingless motor, which reaches high rotational speeds and, in addition, has high magnetic gap capability. In this way, the rotor can operate in a hermetically sealed chamber or in a tube, for example in semiconductor or chemical industries. Possible applications might be pumps, compressors or actuators for high purity chambers [5].

On the one hand, bearingless motors are interesting for high speeds, due to the lack of mechanical bearings. On the other hand, high speeds require small motors. This is challenging with bearingless motors as will be shown in the course of a scale-down.

As for the high speed, a slotless topology is chosen. In conventional bearingless motors, the slots cause higher field harmonics in the rotor and in the stator, which leads to hysteresis and eddy current losses, especially at high speeds. In comparison to existing works [6]–[8], a coil configuration

is used where six toroidally wound coils (cf. Fig. 1) generate both the drive torque as well as the bearing force necessary for levitation of the rotor. This promises a compact design and makes it possible to use a commercial six phase inverter.

A prototype of this topology is already built and tested, but for only 20'000 rpm and with bigger size than intended for the targeted applications. Outgoing from this prototype, a detailed concept for a 150'000 rpm bearingless drive is developed in this paper.

In section II, the working principle of the slotless bearingless drive is explained. The available prototype is introduced in section III. Afterwards, the mechanical stability of the rotor is analyzed for the new concept in section IV to determine the maximal diameter of the rotor for the targeted rotational speed. In section V it is investigated, how the downscaling of the geometry affects the motor and bearing properties of the topology. Thereafter, the influences of magnetic gap length, rotor height and stator height are determined to get an optimal geometry for the high speed drive. In section VII, the detailed geometry is presented and the results are compared to the prototype.

II. THE SLOTLESS BEARINGLESS DISC DRIVE

The slotless bearingless disc drive with toroidal windings is shown in Fig. 1. It has a ring shaped stator, which carries the magnetic flux and therefore has to be manufactured as a stack of sheets. Around the stator, six coils are wound in circumferential direction. The rotor consists of a diametrically magnetized permanent magnet.

A. Passive bearing properties

According to the disc type principle [2], the levitated rotor is passively stabilized against axial displacement and tilting. When the rotor is displaced in z-direction or tilted around the x- or y-axis, passive reluctance forces counteract this displacement (cf. Fig. 2). Therefore, a passive axial stiffness

$$c_z = \frac{dF_z}{dz} \qquad (1)$$

and two tilting stiffnesses

$$c_\alpha = \frac{dT_\alpha}{d\alpha} \text{ and } c_\beta = \frac{dT_\beta}{d\beta}, \qquad (2)$$

can be defined. The angle α defines the rotation around the axis of magnetization and β perpendicular to this axis. As the rotor is magnetized diametrically, the tilting stiffness c_α is smaller than c_β.

However, if the rotor is displaced radially, the attracting forces pull the rotor even farther away from the center. Therefore, the radial stiffnesses

$$c_x = \frac{dF_x}{dx} \qquad (3)$$

in the direction of the magnetization and

$$c_y = \frac{dF_y}{dy}. \qquad (4)$$

perpendicular to the magnetization are destabilizing. This passive radial bearing stiffness has to be compensated by the active magnetic bearing. Without actively controlled bearing forces, no levitation would be possible.
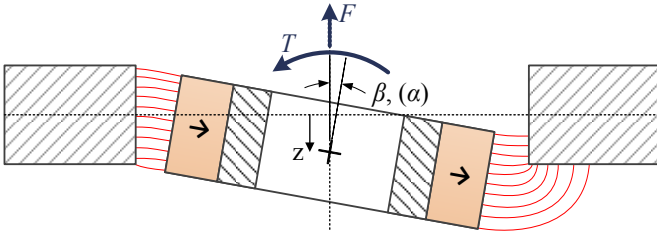

Fig. 2. Stabilizing passive bearing force and torque resulting from axial deflection z and tilting β around axis perpendicular to magnetization.

B. Working principle of the active bearing and drive

The magnetic field in the air gap between the stator and the magnet can be assumed to be ideally in radial direction and with a sinusoidal distribution along the gap perimeter [9]. Therefore, the flux penetrates the wires of the coils at the inner side of the stator perpendicularly. According to the Lorentz force law a force

$$\vec{F} = \int (\vec{J} \times \vec{B})dV \qquad (5)$$

perpendicular to the current density $\vec{J}$ and the magnetic field $\vec{B}$ is generated. This force is always in circumferential direction. If the current of opposite coils flows in the same direction, the force also goes in the same direction on both sides of the rotor. As a result, a bearing force acts on the rotor (cf. Fig. 3). If opposite coils are energized in different directions, the forces also point in opposite directions and a drive torque acts on the rotor. Therefore, both force and torque can be controlled by one set of coils. As two opposing coils can generate a force only in one direction, a second pair is necessary. However, as the air gap field is sinusoidal, in some rotor positions no flux penetrates the coils, so that in this position no force generation in the specified directions is possible. Therefore, six coils have been chosen to be able to generate bearing forces in all directions as well as the drive torque independently of the rotor angle.

To actually control the force and the torque, appropriate current commands for the given assembly have to be found. It proved advantageous to define a three phase current system for the force ($I_{F,1..3}$) and one for the torque ($I_{T,1..3}$).

$$I_{F,1} = \hat{I}_F \cdot \sin(\theta + \varphi_F) \qquad I_{T,1} = \hat{I}_T \cdot \cos(\theta)$$

$$I_{F,2} = \hat{I}_F \cdot \sin\left(\theta - \frac{2}{3}\pi + \varphi_F\right) \quad (6) \qquad I_{T,2} = \hat{I}_T \cdot \cos\left(\theta - \frac{2}{3}\pi\right) \quad (7)$$

$$I_{F,3} = \hat{I}_F \cdot \sin\left(\theta + \frac{2}{3}\pi + \varphi_F\right) \qquad I_{T,3} = \hat{I}_T \cdot \cos\left(\theta + \frac{2}{3}\pi\right),$$

Here, θ is the angle of the rotor, defined by the magnetization axis. $\hat{I}_F$ and $\hat{I}_T$ are the bearing force and motor drive current. This two three phase systems are then superposed on the six coils.
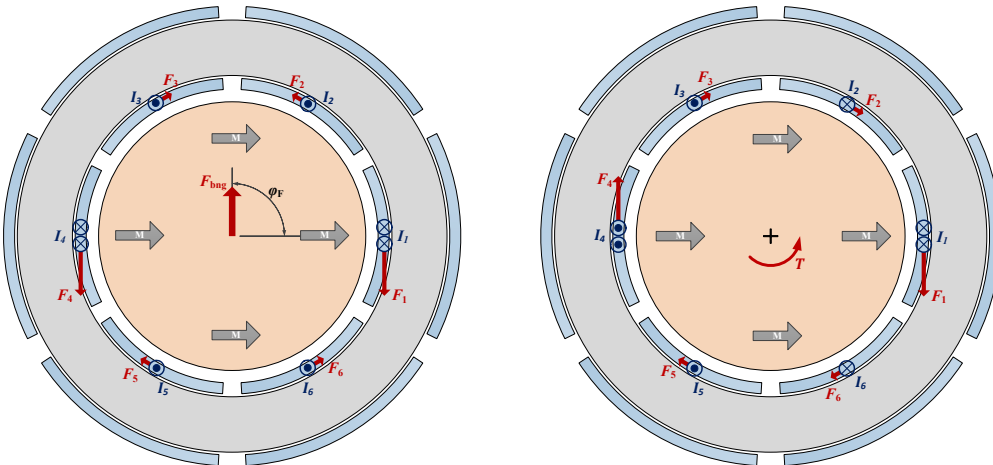

Fig. 3. Principle of bearing force (left) and drive torque generation (right). If the opposite coils are energized in the same direction, the Lorentz forces in the coils also have the same direction and a force acts on the rotor. Energizing the opposite coils in opposite directions results in a torque acting on the rotor.
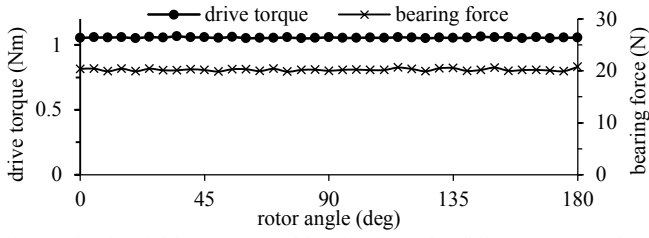
Fig. 4. Simulated drive torque and bearing force for different rotor angles. It shows that generated force and torque are independent of the rotor angle. The bearing and the drive current, respectively, is 750 A·turns. The simulated geometry is the prototype.

$$I_1 = I_{T,1} + I_{F,1} \qquad\qquad I_4 = -I_{T,1} + I_{F,1}$$
$$I_2 = -I_{T,3} + I_{F,2} \qquad\quad I_5 = I_{T,3} + I_{F,2} \qquad (8)$$
$$I_3 = I_{T,2} + I_{F,3} \qquad\quad I_6 = -I_{T,2} + I_{F,3},$$

With simulation results it can be shown, that the resulting bearing force

$$\vec{F} = k_F \cdot \hat{I}_F \begin{pmatrix} \cos(\varphi_F)\,\vec{e}_x \\ \sin(\varphi_F)\,\vec{e}_y \end{pmatrix} \qquad (9)$$

is proportional to the bearing force current. The bearing force coefficient k_F defines the resulting force per applied bearing current. The force angle can be controlled by the phase shift φ_F of the bearing current. In the same way, the proportionality of the torque

$$T = k_T \cdot \hat{I}_T \qquad (10)$$

can be described with the drive torque coefficient k_T. Both force and torque are independent of the motor angle (cf. Fig. 4).

III. CONCEPT OF THE SCALE-DOWN

A. Existing 20 krpm prototype

The starting point of the scale down is an already existing prototype, which proves the feasibility of the bearingless
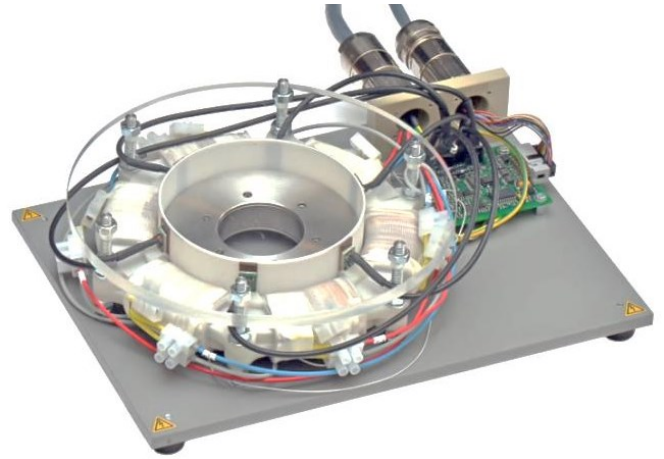

Fig. 5. Picture of the prototype of the slotless bearingless drive. The annular rotor has a diameter of 102 mm. With this prototype, speeds of 20'000 rpm can be reached easily. The speed is limited only by the mechanical strength of the rotor.

motor concept (Fig. 5). The rotor has a diameter of 102 mm. It is ring shaped and has a backiron to reduce the magnet volume.

The rotor can be levitated and rotated up to 20'000 rpm. At low speeds, some resonance frequencies occur, whereas from 3000 rpm onwards no instabilities can be observed. Stable operation at speeds higher than 20'000 rpm would be possible with a stronger rotor. The rotational speed is only limited by the mechanical strength of the rotor.

Fig. 6 shows the measured bearing and drive currents as well as the radial position of the rotor during startup, acceleration, constant speed and deceleration. The acceleration is limited exemplarily to 2000 rpm/s, whereas the deceleration is limited by a drive current limit of 5 A. At low speeds, two resonance frequencies can be seen. During constant speed, the deflection amplitude is around ±70 µm.

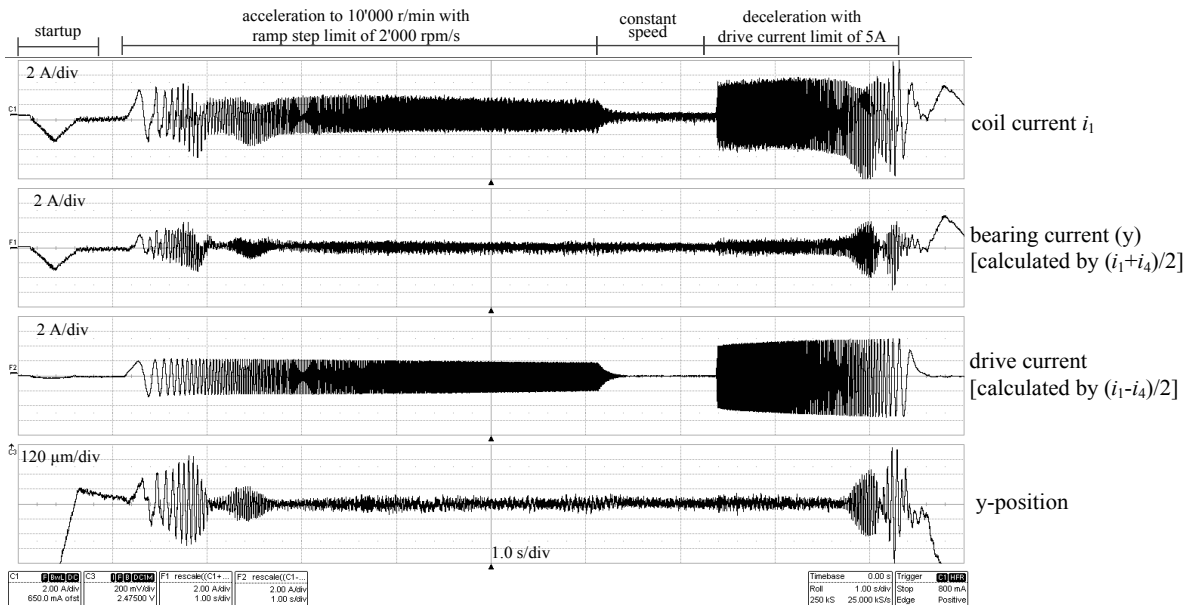During operation, there is a free air gap of 1 mm at each

Fig. 6: Bearing current, drive current and radial position during startup, acceleration to 10'000 r/min and deceleration.

side of the rotor. Six eddy current sensors are located in between the coils to measure the radial position of the rotor, and six hall sensors measure the angular position. A digital signal processor controls two IGBT modules with three half bridges each. Every three coils are connected to a star point and powered by one IGBT module.

Altogether, the feasibility of the proposed topology and the control is proven. The aim is now to decrease the size of the motor to reach higher rotational speeds.

B. Scaling concept for 150 krpm

With the given prototype it appeared that the ring shaped rotor is a weakness in regard to the mechanical strength. Therefore, the rotor in the high speed concept is a solid disc. In the next section, the mechanical stability of this rotor is evaluated. The rotor diameter is chosen to withstand the desired rotational speed.

Then, scaling laws are examined to identify any problems that appear when reducing the size and increasing the speed. As especially the magnetic gap cannot be down-scaled as the rest of the geometry due to manufacturing issues, the influence of the magnetic gap is evaluated in section VI. With that, the geometry of the high speed concept will be defined.

IV. MECHANICAL STABILITY OF THE ROTOR

Special considerations for the mechanical strength of the rotor are necessary to allow high rotational speeds. Several concepts are already available in literature, that allow for circumferential velocities of 180 m/s [10].

The mechanical most problematic part in this topology is the magnet, as it consists of the brittle material NdFeB. To increase the mechanical strength of the rotor compared with the prototype, a disc shaped rotor is chosen. For a rotating disc, the maximal achievable circumferential speed

$$u_{max} = \sqrt{\frac{8}{(3+v)\cdot\rho}\cdot\sigma_S} \qquad (11)$$

is limited only by the tensile strength σ_S and the density ρ of the material [11]. With the given values from the manufacturer ($\sigma_S = 80$ MPa and $\rho = 7500$ kg/m^3) the maximal peripheral speed of the magnet disc results to

$$u_{max} = 161 \text{ m/s}.$$

For the aimed rotational speed of $n = 150'000$ rpm, the maximal diameter of the magnet is

$$D_{max} = \frac{u_{max}}{\pi\,n} = 20.5 \text{ mm}.$$

As this is the maximum, the chosen magnet size for the concept is $D = 20$ mm. Additionally, the magnet will be embedded in two stainless steel shells with a thickness of 1 mm to protect it against collisions. The shell also provides a conductive surface, which serves as target for the eddy current position sensors. However, the shell does not contribute to the overall strength of the rotor, since it slightly bents away from the magnet due to the centrifugal forces. The mechanical strength of the construction has been verified in FE simulations (cf. Fig. 7).
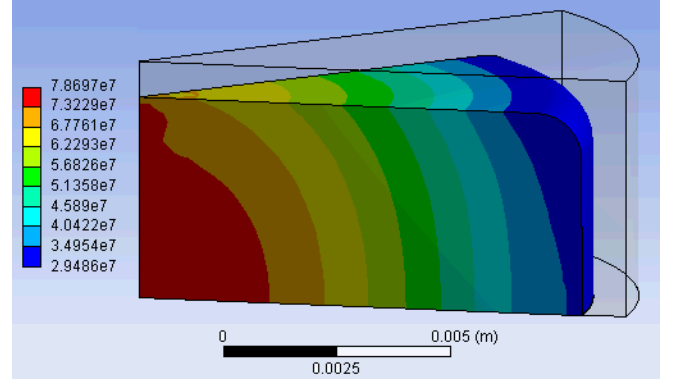

Fig. 7. Distribution of the mechanical tension in the rotor at a speed of 150 krpm, simulated by ANSYS. The rotor consists of a magnet with 20 mm diameter and a stainless steel shell with 1 mm thickness. The picture shows only a section of the upper half of the rotor. The maximal stress in the magnet is 78.7 MPa. Therefore, the rotor will withstand the desired rotational speed.

V. SCALING OF THE GEOMETRY

A. Principle of the scaling

In order to compare the high speed concept with the existing prototype, it is necessary to investigate, how the downscaling will affect the motor and bearing properties. Therefore, in 3D FEM simulations different sizes of the same constellation were simulated and the motor and bearing parameters were examined.

For the scaling of the geometry, the dimensional scaling factor

$$x_d = d_1/d_0 \qquad (12)$$

is introduced, which gives the relation between a new dimension d_1 and the old dimension d_0, whereas all dimensions are scaled simultaneously (i.e. diameter, length, height, air gap, …). In the same way, the speed scaling factor

$$x_n = n_1/n_0 \qquad (13)$$

describes the scaling of the rotational speed n.

The resulting scaling factors for the high speed concept are

$$x_d = {20 \text{ mm}}/{97 \text{ mm}} = 0.206 \qquad (14)$$

for the down-scaling of the magnets and

$$x_n = 150\,000 \text{ rpm}/20000 \text{ rpm} = 7.5 \qquad (15)$$

for the up-scaling of the rotational speed. Here, $x_n \cdot x_d > 1$, because the rotor shape is changed from ring to disc and therefore allows for higher circumferential speeds.

Table I shows results for the relations of selected properties of the motor with the two scaling factors, which will be explained in detail in the following.

B. Active bearing properties

For the active magnetic bearing it is assumed, that occurring disturbance forces F_{dist} only result from mechanical unbalances. Additionally it is assumed, that the masses m_{unb} and radii r_{unb} of the unbalances scale in the same way as all masses and distances in the topology. Therefore, the disturbance forces

$$F_{dist} = m_{unb}\,r_{unb}\,\omega^2 \propto x_d^4\cdot x_n^2 \qquad (16)$$

scale quadratically with the speed and biquadratically with the

dimensional scaling factor. These disturbance forces have to be compensated by the bearing.

Although the magnet changes in size, the magnetic field in the air gap stays constant, because the size of the air gap also changes. However, the simulation shows, that the bearing force coefficient

$$k_{\mathrm{F}} \propto x_{\mathrm{d}} \tag{17}$$

scales linearly with the dimensions. This can be explained with the height of the coils. Each wire inside of the stator carries a current and is penetrated by a B-field, which is independent of the scaling factor. Therefore, the same force per length is generated. As the height of the coils changes linearly with the scaling factor, so does the bearing force coefficient.

As the coil cross sectional area scales quadratically with the size, the current density resulting from the disturbance forces

$$J_{\mathrm{bng}} = \frac{F_{\mathrm{dist}}}{k_{\mathrm{F}} \, A_{\mathrm{coil}}} \propto x_{\mathrm{d}} \cdot x_{\mathrm{n}}^2 \tag{18}$$

goes linearly with the size and quadratically with the speed.

Inserting the values for the downscaling of the prototype it appears, that the current density for the bearing

$$J_{\mathrm{bng,150k}} = 11.6 \, J_{\mathrm{bng,20k}} \tag{19}$$

is more than ten times higher than in the low speed concept.

The copper losses depend on the current density and on the volume V_{Cu} of the coils. With the current density from the bearing currents the copper losses result to

$$P_{\mathrm{Cu,bng}} \propto J_{\mathrm{bng}}^2 \, V_{\mathrm{Cu}} \propto x_{\mathrm{d}}^5 \cdot x_{\mathrm{n}}^4. \tag{20}$$

With the scaling factors for the high speed concept, the copper losses

$$P_{\mathrm{Cu,bng,150k}} \propto 1.18 \cdot P_{\mathrm{Cu,bng,20k}} \tag{21}$$

will rise slightly compared to the bigger prototype. However, the surface of the motor, where heat can be dissipated, is lower by a factor of about 24. Therefore it becomes clear, that the coils in the high speed concept have to be comparatively thicker and more space for the coils has to be allocated in the air gap to reduce the copper losses.

TABLE I:
THE SCALING PROPORTIONALITIES FOR DIFFERENT BEARING AND DRIVE PARAMETERS AND THE VALUES FOR THE DOWNSCALING OF THE PROTOTYPE

Parameter		proportional to	$x_{\mathrm{d}} = 0.206$ $x_{\mathrm{n}} = 7.5$
drive torque coefficient	k_{T}	$\propto x_{\mathrm{d}}^2$	0.0425
drive current density	J_{drv}	$\propto x_{\mathrm{d}}^{-4} \cdot T$	$553 \cdot T$
bearing force coefficient	k_{F}	$\propto x_{\mathrm{d}}$	0.206
disturbance forces	F_{dist}	$\propto x_{\mathrm{d}}^4 \cdot x_{\mathrm{n}}^2$	0.1
bearing current density	J_{bng}	$\propto x_{\mathrm{d}}^{-3} \cdot F_{\mathrm{dist}}$	11.6
eddy current losses	P_{ed}	$\propto x_{\mathrm{d}}^3 \cdot x_{\mathrm{n}}^2$	0.5
hysteresis losses	P_{hy}	$\propto x_{\mathrm{d}}^3 \cdot x_{\mathrm{n}}$	0.07
copper losses	P_{Cu}	$\propto x_{\mathrm{d}}^3 \cdot J$	
translational stiffness	$c_{\mathrm{x,}} c_{\mathrm{y,}} c_{\mathrm{z}}$	$\propto x_{\mathrm{d}}$	0.206
tilting stiffness	$c_{\alpha,} c_{\beta}$	$\propto x_{\mathrm{d}}^3$	0.009

C. Drive properties

For the drive torque coefficient

$$k_{\mathrm{T}} \propto x_{\mathrm{d}}^2 \tag{22}$$

the simulation shows a quadratic dependency on the dimensions. This is because both the generated forces and the distance of forces and rotational axis scale linear. Considering the coil cross-sectional area, the current density for the drive

$$J_{\mathrm{drv}} = \frac{T}{k_{\mathrm{T}} \, A_{\mathrm{coil}}} \propto x_{\mathrm{d}}^{-4} \cdot T \tag{23}$$

rises biquadratically with decreasing size. It now depends on how the load torque is scaled, which is determined by the application. A constant current density can be achieved by also downscaling the torque with x_{d}^4.

The losses of the motor mainly consist of eddy current and hysteresis losses in the stator iron and copper losses in the coils. The eddy current and hysteresis losses depend on the rotational speed n and on the mass m_{S} of the stator.

$$P_{\mathrm{ed}} \propto m_{\mathrm{S}} \, n^2 \propto x_{\mathrm{d}}^3 \cdot x_{\mathrm{n}}^2 \tag{24}$$

$$P_{\mathrm{hy}} \propto m_{\mathrm{S}} \, n \propto x_{\mathrm{d}}^3 \cdot x_{\mathrm{n}} \tag{25}$$

It is evident that the losses per motor volume will stay constant independently of the size. Increase of the speed, however, will rise the loss density. Especially the eddy current losses may get more important over the hysteresis losses at higher speeds.

The copper losses resulting from drive currents

$$P_{\mathrm{Cu,drv}} \propto J_{\mathrm{drv}}^2 \, V_{\mathrm{Cu}} \propto x_{\mathrm{d}}^{-5} \cdot T^2, \tag{26}$$

highly depend on the dimensions and the drive torque. When the drive current density is held constant, the copper losses scale with the volume of the drive and the loss density will stay constant. However, the heat dissipation scales with the surface so that the temperature caused by these losses falls with smaller dimensions. Therefore, a higher drive current density is possible for smaller motors.

D. Passive bearing properties

With the B-field independent of the scaling factor, the passive translational bearing stiffnesses (axial and radial)

$$c_{\mathrm{x}}, c_{\mathrm{y}}, c_{\mathrm{z}} \propto x_{\mathrm{d}} \tag{27}$$

correlate linearly with the dimensional scaling, as they depend on the perimeter of the magnetic gap. As the force coefficient scales in the same way, the destabilizing radial stiffness can be equally compensated independently of the motor size. The weight of the rotor, however, may cause over proportional axial displacement at big motors, as the weight scales with x_{d}^3 much more than the axial stiffness.

The tilting stiffness has the biggest dependency on the scaling,

$$c_{\alpha}, c_{\beta} \propto x_{\mathrm{d}}^3 \tag{28}$$

as it correlates with the power of three. The torque, which counteracts the tilting of the rotor, results from the axial forces at the edge of the rotor. As these forces, the lever to the rotor and the displacement at the rotor edge correlate linear with the scaling factor, the torque has cubic dependency on the scaling.

E. Consequences for High Speed Concept

Summarizing, downscaling of the motor will increase the current density for bearing forces [see (19)]. Therefore it is necessary to increase the coil thickness for the high speed concept. Otherwise, the copper losses may get too high. The density of eddy current and hysteresis losses will stay constant with the size but rise with the speed.

If the motor would be downscaled with a constant circumferential speed, the product of the scaling factors would be $x_d \cdot x_n = 1$. Then, the eddy current losses and the copper losses resulting from the bearing forces would scale linearly with the dimension. Therefore, the loss density rises at downscaling. The hysteresis losses go quadratically with the dimensions and therefore are of less importance for smaller motors. For a constant drive current density, the copper losses $P_{Cu,drv}$ are proportional to the motor volume and are of less importance for smaller motors compared to the iron and bearing copper losses. Besides, constant circumferential speed and constant drive current density results in a constant output power density of the motor.

For downscaling, additional problems arise with the manufacturability and applicability of the motor. The magnetic gap cannot be reduced arbitrarily, as the encapsulation of the rotor and the stator have a minimal thickness. Additionally, the application may require some minimal free air gap, for example if the rotor shall operate in a tube. Therefore, the influence of the magnetic gap will be investigated in the following.

VI. Optimization of the Geometry

A. Magnetic Gap Length

One of the most important decisions for the design of a bearingless drive is the length of the magnetic gap. Depending on the application, a big magnetic gap may be required, for example when the rotor shall be operated in a tube. As the coils are located in the magnetic gap, the coil thickness also determines the gap length. However, the magnetic gap length significantly influences the bearing and motor parameters. The bigger the gap, the smaller is the passive bearing stiffness as well as the drive torque and bearing force.

To investigate the influence of the magnetic gap, FE simulations have been conducted. As the rotor diameter is already fixed at 20 mm, the inner stator diameters d_S has been varied with

$$x_{d_S} = d_S / d_{S,0} \tag{29}$$

starting from $d_{S,0} = 24$ mm.

The outer stator diameter has been increased simultaneously, such that the thickness of the stator stays constant. It shows that all results can be well approximated with power functions, so that they can be compared by their power of relation.

The simulated bearing force is proportional to $x_{d_S}^{-2.16}$ (cf. Fig. 8). This can be explained with the magnetic field, which decreases with the distance to the rotor surface. In [9] the magnetic field in the air gap is calculated analytically. For an infinite relative permeability $\mu_{r,stator}$ in the stator and a $\mu_{r,magnet} = 1$ in the magnet it can be shown, that the magnetic field at the inner side of the stator

$$B \propto \left(\frac{d_{mag}}{d_S}\right)^2 \tag{30}$$

is indirectly proportional to the square of the stator inner diameter and directly proportional to the square of the magnet diameter d_{mag}. As the bearing force is proportional to the magnetic field in the air gap, the force should also correlate to the stator diameter with the power of two. However, taking into account the real material properties as well as the thickness of the coils, the analytical calculation of the dependency results in a proportionality of $x_{d_S}^{-2.13}$, which fits very well with the simulation results.

The torque, however, is proportional to $x_{d_S}^{-0.9}$. As the lever increases with a bigger stator diameter, the torque decreases less than the forces.

As for the small air gap, a small change in the stator diameter means a big change of the magnetic gap length. This can be used to increase the coil area and therefore drastically reduce the current density. This is true because the area of the coil increases far more, than the bearing forces decrease by the required increase of the stator.

However, the increasing magnetic gap drastically reduces the passive stiffnesses of the magnetic bearing (cf. Fig. 9). For the given geometry they depend on the stator radius between $x_{d_S}^{-5.6}$ and $x_{d_S}^{-7}$, as seen in Table II. Especially the tilting stiffness is of importance, as it appeared to be the most critical stability factor in the prototype.

For the high speed concept, a stator diameter of $d_S = 29$ mm is chosen. This is necessary to make the concept manufacturable and to achieve a sufficiently big coil cross-sectional area. The detailed geometry is given in section VII. However, the tilting stiffness is reduced drastically with this increase of the inner stator diameter. Thus, further optimizations of magnet and stator height are necessary, to achieve a tilting stiffness, which is comparable to the prototype.
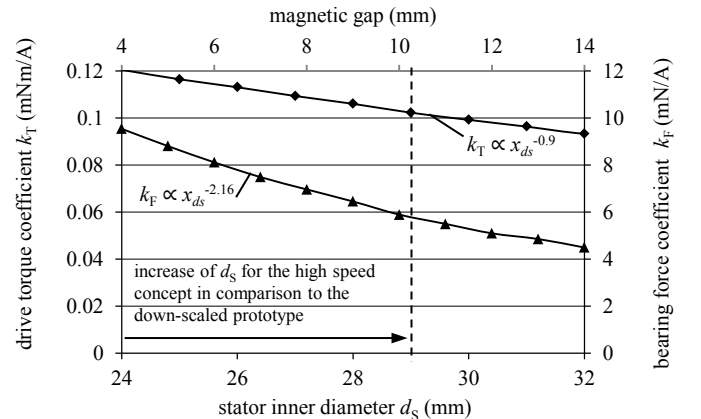

Fig. 8. Drive torque and bearing force simulated for different stator diameters. The results can be approximated by $x_{d_S}^{-0.9}$ (drive torque) and $x_{d_S}^{-2.16}$ (bearing force). The magnet diameter is 20 mm.
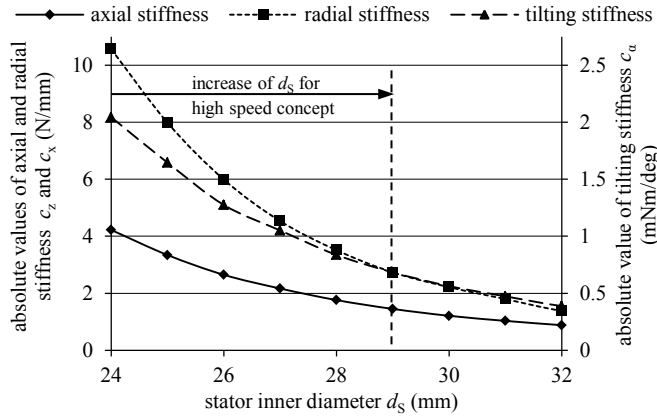
Fig. 9. Passive bearing stiffnesses simulated for different stator diameters. The magnet diameter is 20 mm.

Parameter		proportional to
drive torque coefficient	k_T	$\propto x_{d_S}^{-0.9}$
bearing force coefficient	k_F	$\propto x_{d_S}^{-2.16}$
radial stiffness	c_x, c_y	$\propto x_{d_S}^{-7}$
axial stiffness	c_z	$\propto x_{d_S}^{-5.6}$
tilting stiffness	c_α, c_β	$\propto x_{d_S}^{-6}$

B. Rotor and Stator Height

To optimize the tilting stiffness, different combinations of magnet height and stator height have been simulated with the magnetic gap dimensions of the high speed concept (cf. Table III). It appeared that there is an optimum of the stator height and rotor height (cf. Fig. 10). As it is also explained in [12], the passive tilting stiffness in disc type magnetic bearings is composed of stabilizing axial forces and destabilizing radial forces. The higher the rotor, the bigger are the destabilizing forces, therefore radial magnetic bearings are usually flat. However, when the magnet gets too flat, the magnetic field is weak and the stabilizing axial forces also decrease. Consequently, an optimum exists for rotor and stator height. For the given geometry it appeared that the rotor has to be slightly higher than the stator but smaller than its radius.

For the drive performance it was found, that the drive torque depends linearly on the stator height as well as on the rotor height (cf. Fig. 11). This is true for rotors not much higher than the stator. For higher rotors, saturation effects appear.

VII. COMPARISON OF PROTOTYPE TO HIGH SPEED CONCEPT

As mentioned above, the downscaling of the bearingless motor results in a higher current density in the coils to compensate disturbance forces. Additionally, the size reduction of the magnetic gap will lead to manufacturing problems. Thus, for the high speed drive different geometry proportions have to be chosen than for the lower speed prototype.

A comparison of the original dimensions of the prototype, the dimensions of the prototype downscaled to a magnet
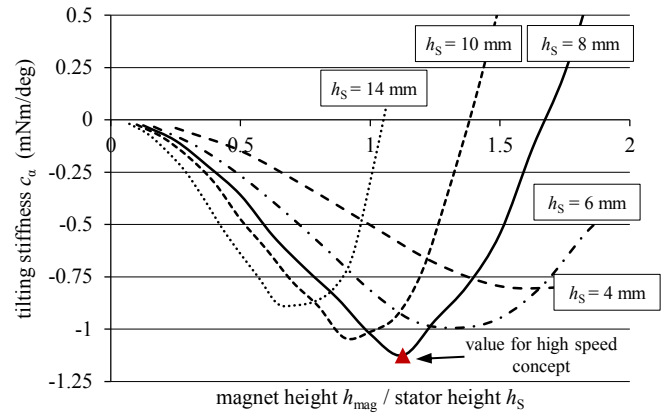

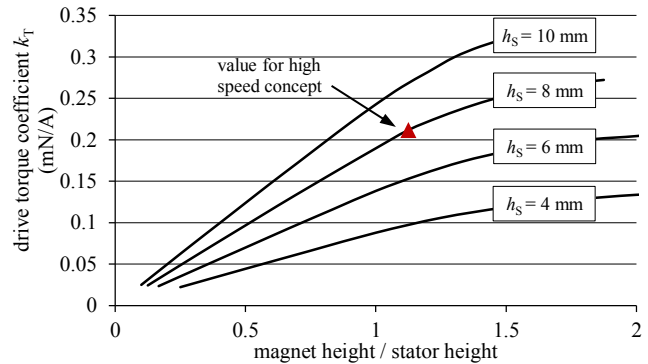Fig. 10. Simulated tilting stiffness depending on magnet height for different stator heights h_S

Fig. 11. Simulated drive torque depending on magnet height for different stator heights h_S
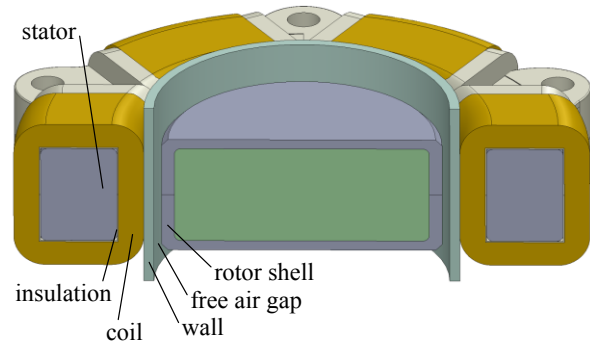

Fig. 12. Cross section of the high speed concept. The magnetic gap consists of the insulation (0.1 mm), the coil (2 mm), the wall (0.8 mm), the free air gap (0.6 mm) and the rotor shell (1 mm)

diameter on 20 mm and the actual high speed concept is given in Table III. The magnet size was reduced to 20 mm to achieve the desired rotational speed. Additionally, the magnet at the high speed concept is a solid disc in contrast to a ring. This leads to a higher magnetic field as well as to higher mechanical strength. The height of rotor and stator is about three times higher compared to the down-scaled prototype to maximize the tilting stiffness and the bearing force and drive torque. Additionally, the magnetic gap is more than twice as big as in the downscaled prototype. Therefore, comparatively thicker coils as well as a thicker wall, free air gap and rotor shell can be used.

As a result, the high speed motor reaches with the same

current density an about ten times higher torque and seven times higher bearing force. This is due to the thicker coil and higher stator and rotor. The translational stiffnesses are also significantly higher. Alone the tilting stiffness is a little bit lower compared to the downscaled prototype, which is due to the bigger magnetic gap. As the magnetic gap is nearly twice as big, the tilting stiffness would be much lower without optimization of rotor and stator height.

VIII. CONCLUSION

Summarizing, an existing prototype for 20'000 rpm was downscaled to reach the desired rotational speed of 150'000 rpm and optimized to overcome the difficulties of the reduced size. As a result, the concept of the bearingless high speed disc motor is producible and may show a stable behavior comparable to the bigger prototype.

TABLE III:
COMPARISON OF GEOMETRY OF HIGH SPEED CONCEPT AND PROTOTYPE

	prototype	scaled prototype[a]	high speed concept[b]	
magnet diameter	97	20	20	mm
inner stator diameter	116	24	29	mm
rotor height	15	3.1	9	mm
stator height	12.5	2.6	8	mm
magnet shape	ring	ring	disc	
total magnetic gap	9.5	2.0	4.5	mm
insulation	1	0.21	0.1	mm
coil	4	0.82	2	mm
wall	1	0.21	0.8	mm
free air gap	1	0.21	0.6	mm
rotor shell	2.5	0.52	1	mm
number of turns	112	112	112	
coil cross-sectional area	190	8.1	24.5	mm^2

[a]Downscaling of the prototype from a magnet diameter of 97 mm to 20 mm

[b]Optimization of scaled prototype according to section VI

TABLE IV:
COMPARISON OF BEARING AND DRIVE PERFORMANCE
OF HIGH SPEED CONCEPT AND PROTOTYPE

	prototype	scaled prototype	high speed concept	
bearing force coefficient	3.05	0.63	1.48	N/A
drive torque coefficient	166	7.05	23.2	mN/A
force per current density	5.17	0.05	0.32	N/ (A/mm^2)
torque per current density	281	0.51	5.08	mNm/ (A/mm^2)
radial stiffness in x	19	3.92	7.22	N/mm
radial stiffness in y	10	2.06	4.9	N/mm
tilting stiffness around x	110	0.96	0.95	mNm/deg
tilting stiffness around y	300	2.63	2.1	mNm/deg
axial stiffness	8.6	1.77	2.26	N/mm

REFERENCES

[1] T. I. Baumgartner, A. Looser, C. Zwyssig, and J. W. Kolar, "Novel high-speed, Lorentz-type, slotless self-bearing motor," in *Energy Conversion Congress and Exposition (ECCE), 2010 IEEE*, 2010, pp. 3971 –3977.

[2] T. Nussbaumer, P. Karutz, F. Zurcher, and J. W. Kolar, "Magnetically Levitated Slice Motors - An Overview," *IEEE Transactions on Industry Applications*, vol. 47, no. 2, pp. 754 –766, Apr. 2011.

[3] S.-M. Yang and M.-S. Huang, "Design and Implementation of a Magnetically Levitated Single-Axis Controlled Axial Blood Pump," *IEEE Transactions on Industrial Electronics*, vol. 56, no. 6, pp. 2213 –2219, Jun. 2009.

[4] T. Reichert, T. Nussbaumer, and J. W. Kolar, "Bearingless 300-W PMSM for Bioreactor Mixing," *IEEE Transactions on Industrial Electronics*, vol. 59, no. 3, pp. 1376 –1388, Mar. 2012.

[5] P. Karutz, T. Nussbaumer, W. Gruber, and J. W. Kolar, "Novel Magnetically Levitated Two-Level Motor," *IEEE/ASME Transactions on Mechatronics*, vol. 13, no. 6, pp. 658 –668, Dec. 2008.

[6] H. Mitterhofer, D. Andessner, and W. Amrhein, "Analytical and experimental loss examination of a high speed bearingless drive," in *2012 International Symposium on Power Electronics, Electrical Drives, Automation and Motion (SPEEDAM)*, 2012, pp. 146 –151.

[7] H. Mitterhofer and W. Amrhein, "Motion control strategy and operational behaviour of a high speed bearingless disc drive," in *6th IET International Conference on Power Electronics, Machines and Drives (PEMD 2012)*, 2012, pp. 1 –6.

[8] H. Mitterhofer and W. Amrhein, "Design aspects and test results of a high speed bearingless drive," in *2011 IEEE Ninth International Conference on Power Electronics and Drive Systems (PEDS)*, 2011, pp. 705 –710.

[9] J. Luomi, C. Zwyssig, A. Looser, and J. W. Kolar, "Efficiency Optimization of a 100-W 500-r/min Permanent-Magnet Machine Including Air-Friction Losses," *IEEE Transactions on Industry Applications*, vol. 45, no. 4, pp. 1368 –1377, Aug. 2009.

[10] A. Binder, T. Schneider, and M. Klohr, "Fixation of buried and surface-mounted magnets in high-speed permanent-magnet synchronous machines," *IEEE Transactions on Industry Applications*, vol. 42, no. 4, pp. 1031 –1037, Aug. 2006.

[11] J. Wittenburg and E. Pestel, *Festigkeitslehre: Ein Lehr- Und Arbeitsbuch*. Springer DE, 2001.

[12] E. Hou and K. Liu, "Tilting Characteristic of a 2-Axis Radial Hybrid Magnetic Bearing," *Magnetics, IEEE Transactions on*, vol. PP, no. 99, pp. 1–1, to be published.